

Experimental nuclear quadrupole resonance and computational study of the structurally refined topological semimetal TaSb₂

T. Fujii,^{1,*} O. Janson,² H. Yasuoka,¹ H. Rosner,¹ Yu. Prots,¹ U. Burkhardt,¹ M. Schmidt,¹ and M. Baenitz¹

¹Max Planck Institute for Chemical Physics of Solids, Nothnitzer Straße 40, 01187 Dresden, Germany

²Leibniz Institute for Solid State and Materials Research IFW Dresden, 01069 Dresden, Germany



(Received 26 September 2023; accepted 12 December 2023; published 9 January 2024)

The local electric field gradients and magnetic dynamics of TaSb₂ have been studied using ¹²¹Sb, ¹²³Sb, and ¹⁸¹Ta nuclear quadrupole resonance (NQR) with density functional theory (DFT) calculations using XRD-determined crystal structures. By measuring all structurally expected 13 NQR lines, the nuclear quadrupole coupling constant (ν_Q) and asymmetric parameter (η) for Ta, Sb(1), and Sb(2) sites were obtained. These values are all in good agreement with the presented DFT calculations. Principal axes of the electric field gradients was determined for a single-crystal sample by measuring the angular dependencies of NMR frequency under a weak magnetic field. The unusual temperature dependence of $\eta(T)$ of Sb(2) hints at the suppressed thermal expansion along the a axis. Spin-lattice relaxation rate ($1/T_1T$) measurements reveal an activated-type behavior and an upturn below 30 K. Neither the low-temperature upturn nor the high-temperature activation-type behaviors are reproduced by the calculated $1/T_1T$ based on the calculated density of states (DOS). On the other hand, the agreement between the calculated DOS and specific heat measurements indicates that the band renormalization is small. This fact indicates that TaSb₂ deviates from the simple semimetal scenario, and magnetic excitations are not captured by Fermi liquid theory.

DOI: [10.1103/PhysRevB.109.035116](https://doi.org/10.1103/PhysRevB.109.035116)

I. INTRODUCTION

Topological insulators and semimetals are receiving tremendous attention in the solid-state research community [1–7]. A spontaneous symmetry breaking via spin-orbit interactions generates a new unconventional phenomenon beyond the Fermi-Landau theory. This required a completely new concept of theoretical description and the introduction of new fermions, the so-called Dirac or Weyl fermions. Dirac and Weyl semimetals have unique electronic structures with linear dispersion in momentum space. The direct experimental proof of this fascinating new physics was achieved by angle-resolved photoemission spectroscopy [8,9]. Indirectly one sees signatures of these topological states formed out of Weyl or Dirac fermions in measurement methods such as resistance (magnetotransport, Shubnikov-de Haas oscillations [10–14]), magnetization (de Haas-van Alphen oscillations [15–17]) or also in the optical conductivity [18–20]. The first Weyl semimetals studied in detail are found among the monpnictides $TMPn$ ($TM = \text{Ta, Nb}$, $Pn = \text{P, As}$) [21]. These systems clearly show the presence of the Weyl nodes near the Fermi level [22]. After the discovery of

superconductivity in Dirac/Weyl monpnictides (TlSb, NbP) [23,24], Weyl dichalcogenides (MoTe₂) [25], and Dirac dipnictides (CaSb₂) [26,27], we extend our studies towards the dipnictides $TMPn_2$ ($TM = \text{Nb, Ta}$, $Pn = \text{P, As, Sb}$). In contrast to the monpnictides, $TMPn_2$ exhibits a centrosymmetric crystal structure. NbAs₂ and TaSb₂ show a negative magnetoresistance [28,29], similar to that observed in TaAs and NbP [13,30]. For the latter compound, this has been claimed to originate from the chiral anomalies in the Weyl fermion. Theoretically, the band structure calculation shows no Weyl fermions in TaSb₂ and there are electron and hole bands, which are not crossing each other [31,32]. Gresch *et al.*, theoretically proposed that the effect of the magnetic field induces the Weyl fermions in $TMPn_2$ [32], that can explain the appearance of negative magnetoresistance. However, the question arises what characteristics of the band structure are formed under a zero magnetic field. A key to understand the physics of these compounds is to examine whether unique topological characters are present under a zero magnetic field.

Using ¹⁸¹Ta nuclear quadrupole resonance (NQR) on TaP, we have succeeded for the first time in detecting the excitations of the Weyl fermions near the Fermi level [33]. In general, the nuclear magnetic resonance (NMR) method has been successfully applied to Dirac/Weyl fermion material under a magnetic fields [34–38], and these experimental results are consistent with theory [39,40]. Ta-based topological semimetals are particularly suitable as Ta has one of the largest quadrupole moments, which facilitates the NQR measurements. Moreover, the NQR method allows us to explore electronic states under a zero magnetic field. In particular, the spin-lattice relaxation rate ($1/T_1$), reflecting the density of

*Takuto.Fujii@cpfs.mpg.de

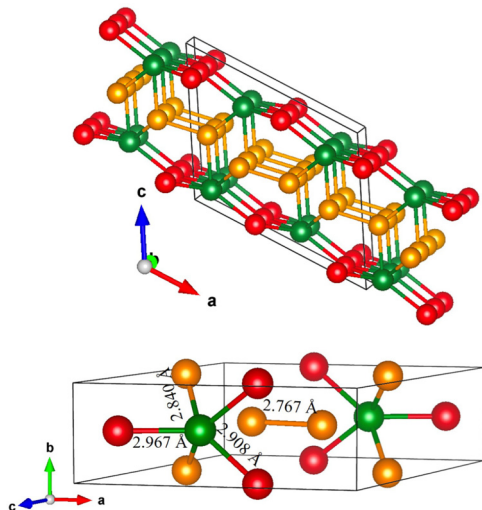


FIG. 1. Monoclinic crystal structure of TaSb₂. There are two inequivalent Sb(1) (red) and Sb(2) (orange), which are bonded to the Ta (green). The cell parameters are $a = 10.233$ Å, $b = 3.648$ Å, $c = 8.303$ Å, $\alpha = \gamma = 90.00^\circ$, and $\beta = 120.40^\circ$ taken from Appendix A.

states (DOS) in nonmagnetic metals and semimetals, has been successfully applied to several Weyl semimetals [33,38].

The aim of this paper is to explore the local electric field gradient and the magnetic excitations in TaSb₂ using mainly the NQR method. Special attention was given to the quality of both the polycrystalline and the single-crystal samples used. Especially in semimetals, it has been known that stoichiometry plays a crucial role. For this reason, detailed investigations by energy dispersive x-ray spectroscopy (EDXS) and structural investigation by x-ray scattering were carried out. We conducted a comprehensive NQR study on the two Sb sites and the Ta site. The temperature dependence of the electric field gradient (EFG) and $1/T_1$ at the two Sb sites and the Ta site have been studied in great detail. Here, we have also conducted single-crystal NMR measurements under a weak field (WFNMR) to check the site assignment of the observed NQR lines and to obtain the EFG tensor experimentally as well. The experimental NQR parameters thus obtained in our detailed study are in rather good agreement with the results of the theoretical calculation based on density functional theory (DFT).

II. CRYSTAL STRUCTURE AND SAMPLE PREPARATION

TaSb₂ crystallizes in the centrosymmetric space group $C2/m$ (NbSb₂-type) and contains two inequivalent Sb(1) and Sb(2) sites, and one Ta site. As shown in Fig. 1, the skeleton of the structure can be viewed as separate units composed by two Ta and two Sb(1) atoms linked by P_σ bonded Sb(2) and Sb(2) dumbbells along the a axis (see Fig. 1). These dumbbells represent a covalent bond between two Sb(2) site. The dumbbell can accommodate four electrons, resulting in an average valence of -2 for the Sb(2) site, while the Sb(1) site has a valence of -3 . Thus the Zintl rule is satisfied. Therefore, it is easily inferred that the electronic and photonic dispersions are highly anisotropic with the a axis being a special axis.

TABLE I. NMR/NQR related nuclear parameters of ¹²¹Sb, ¹²³Sb, and ¹⁸¹Ta.

Isotope	Spin	$\gamma/2\pi$ (MHz/T)	Q (barns)	Natural abundance (%)
¹²¹ Sb	5/2	10.1890	-0.54	57.2
¹²³ Sb	7/2	5.5176	-0.69	42.8
¹⁸¹ Ta	7/2	5.0960	3.17	100

Single crystals were grown by a chemical vapor transport reaction using iodine as a transport agent. TaSb₂ has first been synthesized by a direct reaction of the tantalum (powder 99,98% Alfa Aesar) and antimony (powder 99,999% Alfa Aesar) at 800 °C in a evacuated silica tube during ten days. Starting from this microcrystalline powder, TaSb₂ crystallized by the chemical transport reaction in a temperature gradient from 1000 °C (source) to 950 °C (sink), and a transport additive concentration of 10 mg/cm³ iodine (99,998% Alfa Aesar). The crystallization experiment was carried out in a horizontally arranged two-zone furnace, which was tilted by approximately 10°. The typical size of crystal obtained is 3 × 3 × 1 mm. The quality of the sample was checked by x-ray diffraction measurement. The local stoichiometry was investigated by energy dispersive x-ray (EDX) analysis (see Appendix A). Both data revealed that the synthesized sample is phase pure and of high homogeneity. The TaSb₂ phase was identified half a century ago [41] and its structure assigned to the NbSb₂ type [42]. The roughly atomic coordinates were established from the evaluation of x-ray powder Guinier photographs [43]. Although a detailed description of the crystal structure of TaSb₂ was therefore not yet available, our investigation using x-ray single-crystal diffraction have refined detailed crystal structure (see Appendix A). Hereafter, we will use the refined crystal parameters to analyze NMR data and band structure calculations.

III. NQR AND NMR TECHNIQUES

Our target nuclei in TaSb₂ are ^{121/123}Sb and ¹⁸¹Ta and those nuclear parameters are tabulated in the Table I. The most prominent feature among those parameters is that ¹⁸¹Ta has an extraordinarily large nuclear quadrupole moment. This immediately suggests that ¹⁸¹Ta NQR occurs at a relatively high frequency. The NQR experiments were carried out on powder (crushed single crystals) sample using a conventional pulsed NMR/NQR spectrometer (Tecmag Apollo). The NQR spectra were taken by the frequency-sweep method where the real part of the spin-echo signal was accumulated as a function of frequency. In order to assign the observed NQR lines to nuclear isotopes and different sites, and to determine the principal axes of the EFG tensor, the weak field NMR (WFNMR) measurements were also carried out using an oriented single crystal, where the resonances were obtained under a weak field (less than 0.05 T) applied to the NQR lines. When a weak field applies along the main principal axis of EFG, the NQR lines splits into two lines. We have also measured the angular dependence of the WFNMR lines from where the principal axes of EFG for two Sb sites and one Ta site were determined. The temperature dependence of nuclear spin-lattice relaxation

rate ($1/T_1$) has been measured for the NQR lines by the inversion recovery method. The T_1 values are obtained by fitting the recovery of nuclear magnetization, $M(t)$, measured by the spin-echo amplitude after an application of inversion pulse, to the proper recovery function [refer to Eqs. (B1) and (B2) in Appendix B].

IV. DFT BAND-STRUCTURE CALCULATIONS

First-principles calculations were performed using the full-potential code FPLO ver. 21, employing a local-orbital basis set [44]. To account for the sizable spin-orbit coupling in TaSb₂, we use the full-relativistic treatment. The local density approximation (LDA) parametrized by Perdew and Wang [45] was employed for the exchange-correlation potential. Unless otherwise mentioned, for the structural input we used the data obtained by our x-ray single-crystal diffraction (see Appendix A).

For microscopic insights into the electronic structure of TaSb₂, we resort to the nonmagnetic DOS depicted in Fig. 2(a). The valence band splits into a high-energy manifold dominated by Sb 5*p* states (between -12.5 and -7.5 eV) and the low-energy manifold (starting around -6.5 eV and ranging up to the Fermi energy) to which also Ta 5*d* contributes prominently. The valence and the polarization bands are bridged by a steep valley with an intricate structure. Since this exact shape of this valley plays a crucial role in the transport properties of TaSb₂, we resolve it in the inset of Fig. 2(b). The most prominent feature in this energy range is the dip centered around 0.1 eV above the Fermi energy. The precise structure of the DOS is sensitive to the lattice constants and atomic positions: If we use the optimized TaSb₂ structural from the Materials Project (mp-11697 [46]), this dip becomes sharper and moves closer to the Fermi level. Moreover, the difference between scalar-relativistic and full-relativistic calculations reveals a profound impact of the spin-orbit coupling (SOC) on the electronic structure in this energy range. Interestingly, if we consider the full valence band, this difference becomes barely visible [Fig. 2(b), main panel].

It has been suggested that a magnetic field may stabilize a Weyl point in TaSb₂ [32]. While we can not exclude such scenario, the band structure plot reveals that highest-lying occupied band and the lowest-lying unoccupied band are separated by a finite gap [Fig. 2(c)]. Since the magnetic energy scale is roughly set by Bohr magneton, which amounts to approximately 5.8×10^{-5} eV/T, closing a gap of 0.1 eV would require an unrealistically large magnetic field.

V. RESULTS AND DISCUSSION

A. NQR spectra and site assignment

Searching for the NQR signal in TaSb₂, we consider the splitting of nuclear energy levels due to the quadrupole interaction, which is expressed by the following Hamiltonian,

$$H_Q = \frac{h\nu_Q}{6} \left[(3I_z^2 - I^2) + \frac{1}{2}\eta(I_+^2 + I_-^2) \right], \quad (1)$$

where h is Planck's constant, ν_Q is the nuclear quadrupole coupling constant, $\eta = |V_{xx} - V_{yy}|/|V_{zz}|$ is the asymmetric parameter, V_{xx} , V_{yy} , and V_{zz} are the EFG at nuclear sites along

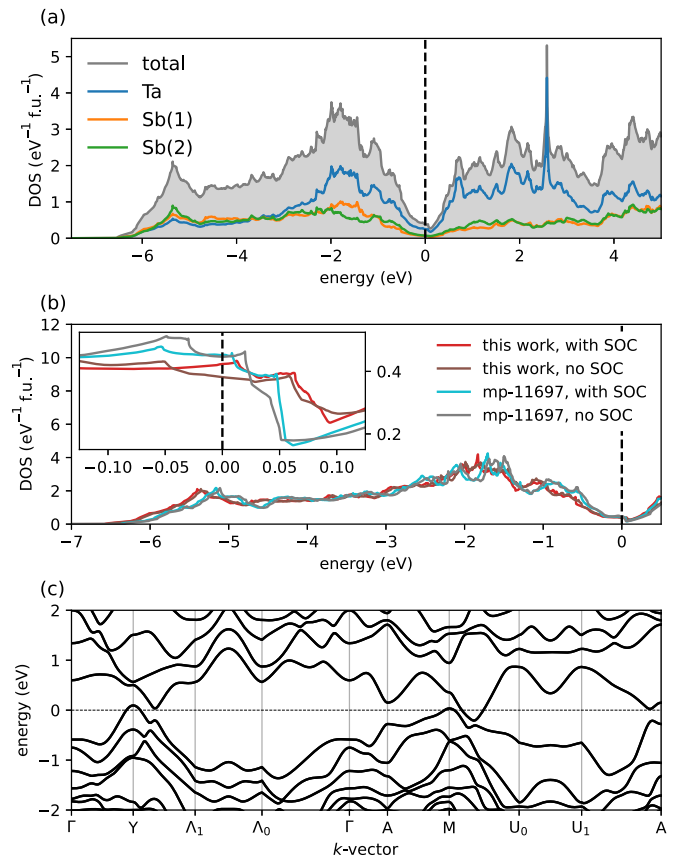


FIG. 2. Electronic structure of TaSb₂ in nonmagnetic LDA calculations. (a) Total and site-resolved density of states (DOS) in a full-relativistic nonmagnetic calculation. (b) Comparison of DOS calculated in the full relativistic (with SOC) and scalar-relativistic (no SOC) mode for two structures: the experimental structure obtained from our x-ray single-crystal diffraction (see Appendix A) and the optimized structure from the Materials Project (mp-11697 [46]). The inset shows a blow up of the same data. (c) Band structure for the experimental crystal structure. In all plots, the Fermi level (dashed line) is at zero energy.

the x , y , and z axis, respectively. Here, we note that the z axis is the maximum principal axis of the EFG tensor, V_{zz} , and nuclear spins are quantized along V_{zz} at zero field. The quadrupole-split nuclear energy levels E_m and the resulting transition frequencies can easily be calculated numerically by diagonalizing Eq. (1). For $\eta = 0$, the energy levels can be expressed as

$$E_m = \frac{h\nu_Q}{6} [3m^2 - I(I+1)], \quad \nu_Q = \frac{3eQ|V_{zz}|}{h2I(2I-1)}. \quad (2)$$

Then the NQR frequency can be written as $\nu_{NQR} = \nu_Q(2|m| + 1)/2$, because the NQR occurs for the transition between two levels $|m|$ and $|m+1|$. Therefore, for $\eta = 0$, two and three NQR lines with equal spacings are expected for $I = 5/2$ and $I = 7/2$, respectively. For $\eta \neq 0$, those NQR lines will be shifted with unequal spacing [47]. Hence, a total of 13 NQR lines should be observed for ¹²¹Sb(1), ¹²³Sb(1), ¹²¹Sb(2), ¹²³Sb(2), and ¹⁸¹Ta sites in TaSb₂. In Figs. 3(a)–3(c), we show the observed NQR spectra at 5 K. The expected 13 NQR lines have clearly been observed in the frequency range of

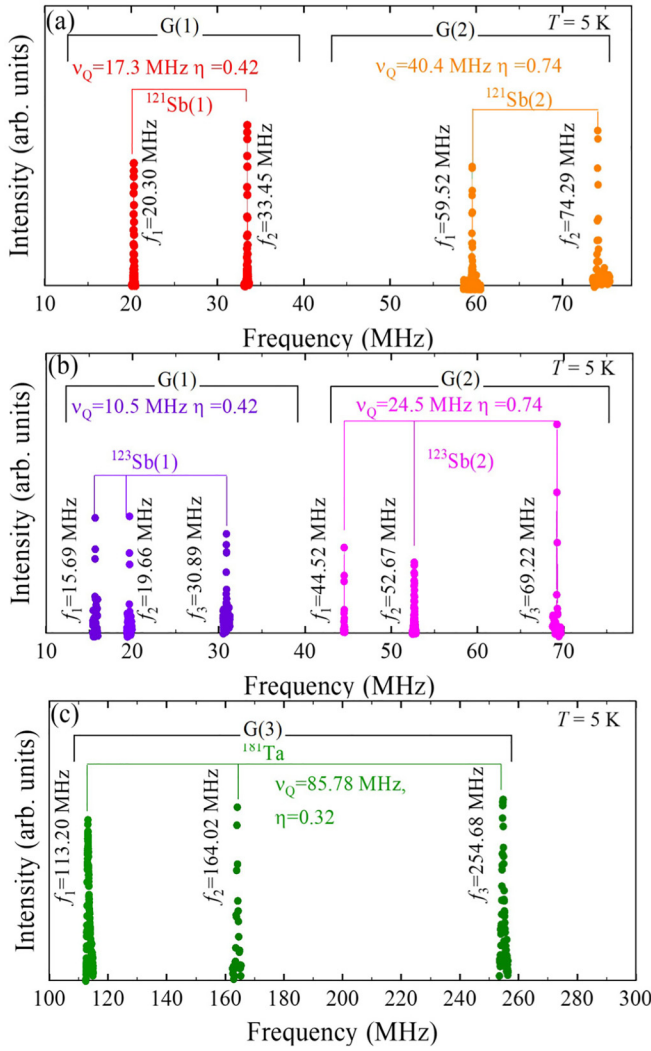


FIG. 3. (a) ^{121}Sb , (b) ^{123}Sb , and (c) ^{181}Ta -NQR spectra of TaSb_2 at 5 K. There are three groups of NQR spectra, G(1), G(2), and G(3), which are assigned to Sb(1), Sb(2), and Ta sites. The lines f_1 , f_2 , and f_3 correspond to $\pm 3/2 \leftrightarrow \pm 1/2$, $\pm 5/2 \leftrightarrow \pm 3/2$, and $\pm 7/2 \leftrightarrow \pm 5/2$ transitions, respectively.

10 ~ 260 MHz. The peak frequencies for each line have been obtained by fitting each line to a Gaussian function.

The following procedures have been taken for the site assignment, namely how we can associate each line to the particular sites and nuclear isotopes. First, we consider the nuclear quadrupole moment (Q) for each nucleus to assign which site the spectrum originated from. The Q of ^{181}Ta ($^{181}Q = 3.170 \times 10^{-28} \text{m}^2$) is approximately five times larger than that of $^{121/123}\text{Sb}$ ($^{121}Q = 0.543 \times 10^{-28}$ and $^{123}Q = 0.692 \times 10^{-28} \text{m}^2$). Moreover, the $^{121/123}\text{Sb}$ NQR lines at the same site are expected to be observed in a close frequency range since the ratio of $^{121}\nu_Q$ to $^{123}\nu_Q$ at the same site is 1.47 from Eq. (2). Here, for the sake of clarifying, the observed NQR lines are divided into three groups according to frequency ranges of observed NQR lines and assigned as G(1) (15 ~ 40 MHz) for $^{121/123}\text{Sb}$, G(2) (40 ~ 75 MHz) for $^{121/123}\text{Sb}$, G(3) (110 ~ 255 MHz) for Ta.

TABLE II. Experimental results and calculated EFG tensor V_{zz} , quadrupole coupling ν_Q and asymmetry parameter η for each site in TaSb_2 . Sb(1) and Sb(2) are inequivalent Sb sites and the labeled one is consistent with the one named for the crystal structure.

	Experiment		Calculation		
	ν_Q (MHz)	η	V_{zz} (10^{21}V/m^2)	ν_Q (MHz)	η
$^{121}\text{Sb}(1)$	17.3	0.42	-7.371	14.5	0.45
$^{123}\text{Sb}(1)$	10.5			8.8	
$^{121}\text{Sb}(2)$	40.4	0.74	-18.391	36.2	0.88
$^{123}\text{Sb}(2)$	24.5			22.0	
^{181}Ta	85.78	0.32	-15.147	82.9	0.22

Next, we estimate the ν_Q from the combinations of all spectra within each group. The estimated ν_Q for ^{121}Sb and ^{123}Sb at each site should correspond to each other when the site assignment is correct. Here, we also consider the asymmetry parameter η because the peak frequencies are unequally spaced for any combinations of spectra. In order to estimate the values of ν_Q and η from the observed peak frequencies at 5 K, a least-squares analysis was performed using theoretical quadrupole interaction obtained from the exact diagonalization. The values of ν_Q and η have been estimated from all combinations of NQR lines within each group. We found the combinations of NQR lines in which the ν_Q and η for ^{121}Sb correspond to that for ^{123}Sb , as shown in Table II. Therefore we conclude that G(1), G(2), and G(3) are associated with, respectively, Sb(1), Sb(2), and Ta sites.

The quadrupolar frequency ν_Q and the asymmetry parameter η can be obtained from the EFG tensors at nuclear sites defined as the second partial derivative of the electrostatic potential $v(r)$ at the position of the nucleus:

$$V_{ij}(r=0) = \left(\frac{\partial^2}{\partial i \partial j} v(0) - \frac{1}{3} \delta_{ij} \nabla^2 v(0) \right), \quad (3)$$

where δ_{ij} and ∇^2 are the Kronecker delta and the Laplace operator, respectively. In the DFT calculation, we choose Ta ($4f/5s5p6s5d6p5f$) and Sb ($4s4p4d/5s5d5p4f$) semicore/valence states as a basis set. The inclusion of higher-lying states into the basis is crucial for an accurate estimation of the EFG tensor [33]. The calculated ν_Q and η are provided in Table II next to the experimental values. Experimentally obtained values of ν_Q and η are in good agreement with the calculated values within 16%. This result assures that our line assignment to the site and isotope is correct. As a side remark, we note that η is a relative measure, and its distribution law differs from that of individual EFG components. Assuming that the latter are normally distributed, the distribution of η can be approximated as normal, even though with the ~ 1.5 times larger standard deviation. This difference has to be taken into account for a proper comparison.

B. Weak field NMR and determination of the principal axis

To experimentally determine the principal axes of the EFG tensor, a weak magnetic field (H) was applied to the single crystal. Here, we can treat the Zeeman term $H_z = -\gamma_N H (I_x \sin \theta \cos \phi + I_z \cos \theta)$ as the perturbation of H_Q , where θ and ϕ are the angle between a magnetic field and

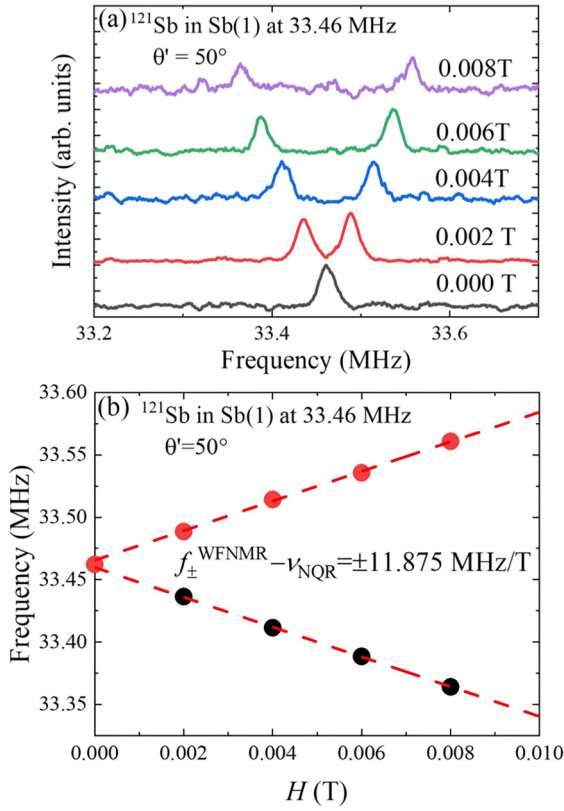


FIG. 4. Typical example of the field dependence of (a) WFNMR spectra and (b) peak frequencies for ^{121}Sb at 33.46 MHz NQR line. The weak fields were applied along $\theta' = 50^\circ$. The slope is estimated as 11.875 MHz/T (see main text). Note that the bare gyromagnetic ratio of ^{121}Sb is 10.189 MHz/T.

the principal axis of V_{zz} in the x - z plane and x - y plane, respectively, and γ_N is the bare nuclear gyromagnetic ratio. Then one NQR line splits into two lines (f_{-m}^{WFNMR} and f_{+m}^{WFNMR}). In the case of transitions between $\pm 1/2$ and $\pm 3/2$, transitions between m and $m \pm 2$ also occur, so that exceptionally one NQR line splits into four lines [47]. Therefore, generally six and eight WFNMR lines are expected for $I = 5/2$ and $7/2$, respectively (see detail in Appendix C). We define the splitting width $\Delta f = f_{-m}^{\text{WFNMR}} - f_{+m}^{\text{WFNMR}} = 2\gamma'H$ where γ' is an apparent nuclei gyromagnetic ratio and the Δf exhibits an angular dependence (see detail in Appendix C). The typical example of the WFNMR spectra at $^{121}\text{Sb}(1)$ ($\nu_{\text{NQR}} = 33.46$ MHz) is shown in Fig. 4(a). The clear splitting of the spectrum has been observed. The peak frequencies for each magnetic field have been obtained by fitting each spectrum to two Gaussian functions. The line width of the spectra does not vary with the magnetic field and no additional peaks were observed. This fact indicates that magnetism or magnetic impurities are absent. As shown in Fig. 4(b), the field dependence of peak frequencies is linear, and the slope is 11.875 MHz/T at $\theta' = 50^\circ$, where θ' is an angular between the magnetic field and the axis perpendicular to the c axis in the ac plane. The slope greater than $\gamma = 10.189$ is due to the effect of finite η .

The principal axis of V_{zz} and the associated isotope can be assigned by examining the angular dependence of $\Delta f/2H$ [$\Delta f/2H(\theta')$]. We have measured the angular

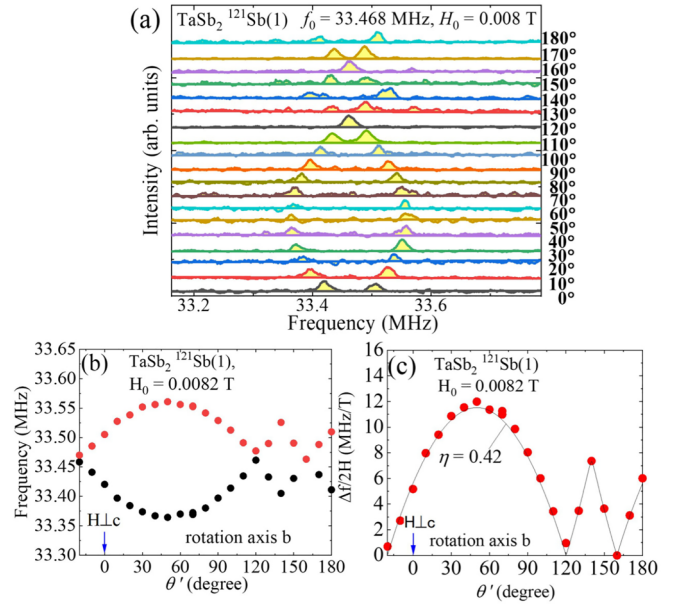


FIG. 5. Typical example of the angular dependence of $^{121}\text{Sb}(1)$ WFNMR frequency. (a) FFT spectra taken at 33.46 MHz and 0.0082 T external field. Here a single crystal was rotated along the b axis. (b) Angular dependence of peak frequency of the spectra. (c) Angular dependence of $\Delta f/2H$ extracted from exact diagonalization. Solid lines are data fits to theoretical $H_Q + H_z$ from exact diagonalization where $\nu_Q = 17.5$ MHz and $\eta = 0.42$ were obtained.

dependence of WFNMR at the highest NQR frequency lines for G(1) and G(2) and the f_2 line for G(3). For example, the angular dependence of WFNMR spectra and peak frequencies for $^{121}\text{Sb}(1)$ are shown in Figs. 5(a) and 5(b), respectively. Also, the angular dependence of $\Delta f/2H$ is shown in Fig. 5(c). We found that the principal axis of V_{zz} for Sb(1) is pointing $\theta' = 50^\circ$, $\phi' = 0$ and $\eta = 0.42$, where ϕ' is the angle between the principal axis of V_{zz} and the ac plane. Note that $\phi' = 0$ means that V_{zz} being within the ac plane.

Similar measurements were made at $^{121}\text{Sb}(2)$ and ^{181}Ta , then we have found that the principal axis of V_{zz} pointing $\theta' = 107^\circ$ and 125° , $\phi' = 0$ and 0 , $\eta = 0.74$ and 0.32 , respectively. The obtained η values are consistent with the experimental values obtained from the satellite structure shown in Table II. From the DFT calculation, we have obtained the direction of the principal axis of V_{zz} as $\theta' = 69^\circ$, 122° , and 135° for Sb(1), Sb(2), and Ta sites, respectively. Therefore, the experimentally obtained direction of principal axis of V_{zz} is in good agreement with the theoretical one.

C. Temperature dependence of ν_Q and η

In order to extract the temperature dependence of the quadrupolar parameters, ν_Q and η , the temperature dependence of the NQR frequencies for all lines have been measured up to 250 K. The results are shown in Figs. 6(a), 6(c) and 6(e). The $\nu_Q(T)$ at each site follows an empirical $\nu_Q(0)(1 - AT^{3/2})$ law below 50 K. This is a typical temperature dependence reflecting the temperature dependence of thermal expansion [48]. From the least-squares fit of $\nu_Q(T)$ to $\nu_Q(0)(1 - AT^{3/2})$, we obtained the $\nu_Q(0)$ at each site, as

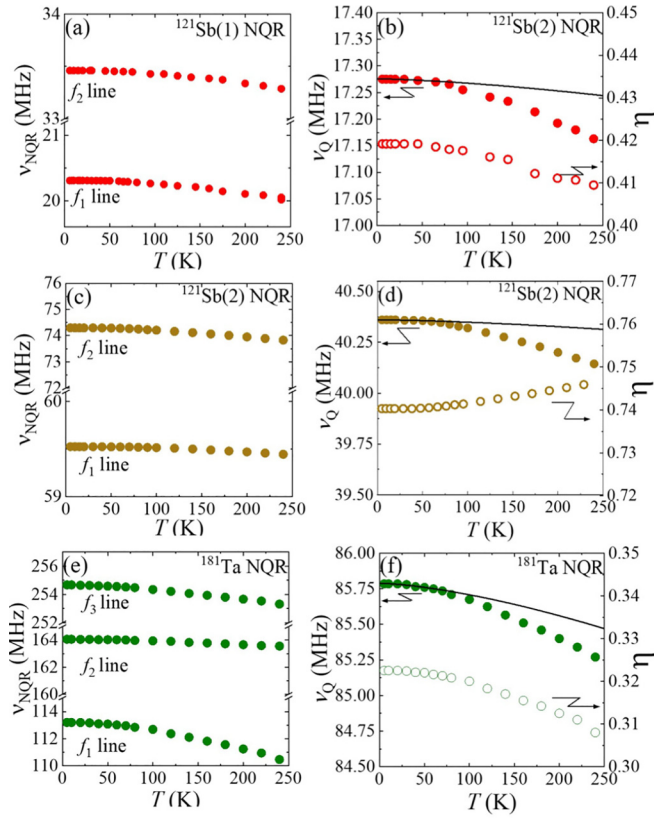


FIG. 6. (a), (c), and (e) temperature dependences of NQR frequency for $^{121}\text{Sb}(1)$, $^{121}\text{Sb}(2)$, and ^{181}Ta , respectively. (b), (d), and (f) temperature dependence of ν_Q and η for $^{121}\text{Sb}(1)$, $^{121}\text{Sb}(2)$, and ^{181}Ta , respectively. The black solid lines represent the fits of the $\nu_Q(T)$ using $\nu_Q(0)(1 - AT^{3/2})$ below 50 K.

shown in Figs. 6(b), 6(d) and 6(f). To discuss site dependence of EFG, the fractional decrease of $V_{ii}(T)$ ($i = x, y, z$), $\Delta V_{ii}(T) = [V_{ii}(0) - V_{ii}(T)]/V_{ii}(0)$ are shown in Figs. 7(a), 7(b) and 7(c). The deviation in $\Delta V_{zz}(T)$ among sites is less than 0.06% over the whole temperature range, and there is hardly seen any site dependence on $\Delta V_{zz}(T)$. In contrast, $\eta(T)$ show different behavior depending on the site: at the Sb(1) and Ta sites, the $\eta(T)$ decreases with increasing temperature, whereas at the Sb(2) site, $\eta(T)$ increases [see Fig. 6(d)].

The site differentiation might be due to the anisotropy of the thermal expansion of lattice parameters. Here we extract V_{xx} and V_{yy} (see detail in Appendix D) to discuss $\eta(T)$ in more detail at each site. Figures 7(a) and 7(b) show the $\Delta V_{xx}(T)$ and $\Delta V_{yy}(T)$ for each site, respectively. First, as a characteristic behavior, both ΔV_{xx} and ΔV_{yy} depend on temperature at the Sb(1), whereas ΔV_{yy} almost no temperature dependence was observed at the Sb(2). The temperature independent of ΔV_{yy} is the main source of the unusual increase of $\eta(T)$. Based on the DFT calculation, only ΔV_{yy} for Sb(2) is pointing to a axis, as shown in Fig. 7(e). This result indicates that the lattice thermal expansion of the a axis might be smaller than the others. Next, the ΔV_{yy} for Sb(1) and Ta and ΔV_{xx} for Sb(2), pointing to the b axis, are increasing, that indicates thermal expansion induces in the b -axis direction. The temperature dependence of EFG tensors pointing in the ac plane demonstrates that ΔV_{zz} shows an increase with increasing temperature at all sites, whereas

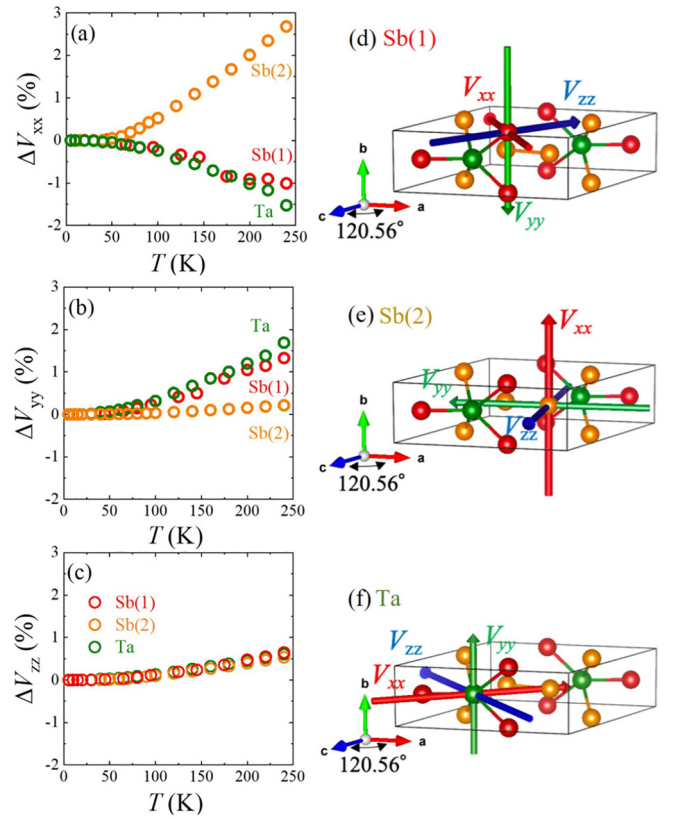


FIG. 7. Fractional temperature dependence of (a) $\Delta V_{xx}(T) = [V_{xx}(0) - V_{xx}(T)]/V_{xx}(0)$, (b) $\Delta V_{yy}(T) = [V_{yy}(0) - V_{yy}(T)]/V_{yy}(0)$, and (c) $\Delta V_{zz}(T) = [V_{zz}(0) - V_{zz}(T)]/V_{zz}(0) = \Delta \nu_Q(T)$. The directions of EFG principal axis V_{xx} (red arrow), V_{yy} (green arrow), and V_{zz} (blue arrow) are illustrated for (d) Sb(1) site, (e) Sb(2), (f) Ta site.

ΔV_{xx} shows a decrease at Sb(1) and Ta. If one considers thermal expansion as the sole cause of these temperature dependencies, a contradiction arises because ΔV_{zz} indicates an expansion and V_{xx} indicates a shrinkage. For a deeper insight into the mechanism of thermal expansion, low-temperature diffraction experiments and dilatometry studies are highly recommended.

D. Temperature dependence of $1/T_1$

Before discussing the temperature dependence of $1/T_1$ based on the band structure, it is necessary to clarify that the relaxation process is governed by the magnetic excitations, rather than the quadrupolar process. One way of doing this is the careful analysis of the recovery of the nuclear magnetization from the saturated state to the thermally equilibrium state. From the recovery of nuclear magnetization, it was confirmed that the relaxation process is governed by magnetic excitation (see detail in Appendix B). Furthermore, the experimentally obtained T_1 ratio between ^{121}Sb and ^{123}Sb , $^{121}T_1 / ^{123}T_1$, is a good measure of whether the relaxation process is governed by magnetic or quadrupolar, because the former case the ratio should be $(^{123}\gamma_N / ^{121}\gamma_N)^2 = 0.29$ while the latter case it should be $(^{123}Q / ^{121}Q)^2 = 1.62$. We have obtained the experimental ratio of 0.30 and 0.29 at Sb(1) and Sb(2), respectively. These values agree well with the $(^{123}\gamma_N / ^{121}\gamma_N)^2$. From the

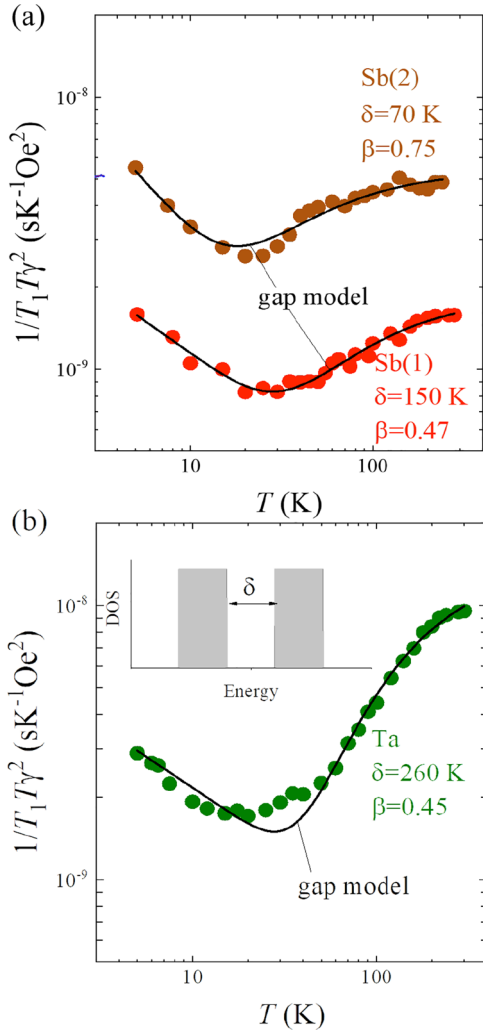


FIG. 8. Temperature dependence of $1/T_1 T \gamma_N^2$ for (a) ^{121}Sb at Sb(1), Sb(2) and (b) ^{181}Ta . The solid lines are the data fits to Eq. (7) with parameter $\delta = 150$ K, 70 K, and 260 K for Sb(1), Sb(2), and Ta, respectively. Inset: The model of density of states with gap δ .

above two evidences, we are strongly confident that the relaxation process in TaSb_2 is to be discussed from magnetic excitations.

Putting the experimentally obtained temperature dependence of Q_n and K_n due to those of $\eta(T)$ [see Figs. 6(b), 6(d) and 6(f)] to Eqs. (B1) and (B2) in Appendix B, we have obtained the temperature dependence of $1/T_1 T$ for the f_2 ($\pm 3/2 \Leftrightarrow \pm 5/2$) line of ^{121}Sb at Sb(1) and Sb(2) sites, and f_2 ($\pm 3/2 \Leftrightarrow \pm 5/2$) line of ^{181}Ta at Ta site. The obtained results are shown in Fig. 8.

where the $1/T_1 T$ are divided by the square of the γ_N to eliminate nuclear specific parameter. Although the general feature has been seen in many semimetallic materials, one can immediately observe that there exists a characteristic temperature, $T^* \approx 30$ K, where the relaxation process has a crossover from a high-temperature activation-type behavior, which is presumably associated with the excitations to a higher unoccupied state to a low-temperature modified Korringa excitations.

Among topological materials, especially in the Dirac/Weyl fermion system with linear band dispersions, a power-law

behavior $1/T_1 T \sim T^n$ has been observed at high temperatures [33,38]. The power-law behavior originated from a Fermi-contact and/or an orbital contribution of hyperfine interaction. When the Fermi-contact contribution is dominant, T^4 dependence is predicted due to the linear dispersion with the point node. While when the orbital contribution is dominant, an unusual temperature dependence of hyperfine interaction leads to a T^2 dependence in $1/T_1 T$ [40,49]. However, neither case can explain the activation-type behavior. This result is consistent with the absence of Weyl points at zero magnetic field in TaSb_2 from band-structure calculations.

Quite generally, $1/T_1 T$ can be expressed by using the wave-vector- (q) and frequency- (ω) dependent magnetic susceptibility, $\chi(q, \omega)$, characterizing the magnetic excitations in a system as [50,51],

$$\frac{1}{T_1 T} = \frac{2\gamma_N^2 k_B}{g^2 \mu_B^2} \sum_q A_q^2 \frac{\chi''_{\perp}(q, \omega)}{\omega_N}, \quad (4)$$

where $\chi''_{\perp}(q, \omega)$ is the transverse component of imaginary part of $\chi(q, \omega)$, A_q is the q -dependent hyperfine coupling constant and ω_N is the frequency for the NQR. Since at the moment we do not have a plausible microscopic theory to calculate the $\chi(q, \omega)$ in multiband systems such as TaSb_2 , we have adopted the theoretical $1/T_1 T$ for noninteracting itinerant electrons based on the band structure calculation with random phase approximation (RPA). For such a system $1/T_1 T$ is expressed using the density of state near the Fermi level as [52],

$$\frac{1}{T_1 T} \propto \frac{A_{hf}^2}{T} \int f(E - \mu_c)[1 - f(E - \mu_c)]\{D(E)\}^2 dE, \quad (5)$$

where $f(E)$ is a Fermi distribution function, $D(E)$ is the energy-dependent density of state and $\mu_c(T)$ is the temperature-dependent chemical potential. Were there no change of A_{hf} with temperature, the calculation of $1/T_1 T$ is straightforward from calculated $D(E)$ [see Fig. 2(a)]. At all sites, the calculated $1/T_1 T$ shows a constant value without increase. Namely, neither the low-temperature upturn nor the high-temperature activation-type behaviors are reproduced by the calculated $1/T_1 T$ based on the DOS. The absence of sharp DOS features in the immediate vicinity of the Fermi level excludes the possibility of sizable shifts of the μ_c (and hence the DOS at μ_c) at low temperatures. Thus, the nature of the experimentally observed upturn in $1/T_1 T$ remains elusive in the band structure. One possible explanation is that the DFT fails to describe the electronic structure of TaSb_2 accurately. While deficiencies of DFT can not be excluded especially for highly covalent systems, we have two arguments that render such a scenario unlikely. First, our DFT calculations accurately describe the EFG tensors. Second, our results are in agreement with the linear coefficient $\gamma = 1.2 \text{ mJ mol}^{-1} \text{ K}^{-2}$ estimated from the Sommerfeld expansion of the specific heat at low temperatures (see Appendix E). Indeed, γ can be estimated directly from the DOS at the Fermi energy D_{ϵ_F} (in J^{-1} per formula unit)

$$\gamma_{\text{DFT}} \left[\frac{\text{mJ}}{\text{mol} \cdot \text{K}^2} \right] = \frac{k_B^2 \pi^2 N_A V_{\text{uc}}}{3} D_{\epsilon_F} \times 10^3, \quad (6)$$

where k_B is the Boltzmann constant (in J/K), N_A is the Avogadro number (in mol⁻¹), $Z = 2$ is the number of formula units per cell, and V_{uc} is the unit cell volume (in m³). In the full relativistic calculations, the resulting γ_{DFT} values amount to 1.00 ± 0.05 mJ mol⁻¹ · K⁻². We also simulated the very small possible deviation of the sample stoichiometry from the ideal 1:2 ratio (see Appendix A) applying the virtual crystal approximation and found no significant changes in the DOS near the Fermi level. The agreement between the calculated and the experimental values also not only supports our DFT analysis, but also indicates that band renormalization in TaSb₂ is small. The discrepancy between the experimental $1/T_1T(T)$ and those from the band structure calculation demonstrate that TaSb₂ is not a simple semimetal, and the magnetic excitation has to be treated beyond the simple Fermi liquid scenario.

Following a number of previous NMR studies such as SmB₆ [53], PuB₄ [54], and FeGa₃ [55], we assume an existence of rather arbitral in-gap state, which is invisible in calculated band structure to analyze the $1/T_1T$. Here, $D(E)$ exhibits a symmetric band gap δ centered at E_F shown in inset of Fig. 8(b). The origin of the narrow band in-gap state is not clear but may be associated with the Anderson localization or impurity states. Assuming a simple in-gap state with narrow bands, which is invisible in the calculated band structure, the activation-type temperature dependence of $1/T_1T(T)$ is discussed by a phenomenological way. The data are then fitted to the following empirical equation, including the upturn at low temperatures,

$$\frac{1}{T_1T} = \alpha T^{-\beta} + \left(\frac{1}{T_1T}\right)_0 \exp\left(-\frac{\delta}{2k_B T}\right). \quad (7)$$

The first term describes a fluctuation of the localized electron moments within the narrow band at low temperatures, and the second term describes thermal excitation of the quasiparticles. The solid lines in Figs. 8(a) and 8(b) indicate such fit of the $1/T_1T(T)$ to Eq. (7) with $\delta = 13$ meV (150 K), 6 meV (70 K), and 23 meV (260 K) for Sb(1), Sb(2), and Ta sites are obtained, respectively. The obtained different activation energies at each site might indicate the presence of site-dependent gap. As indicated by the site dependence of the gap size, the increase of $1/T_1T$ with temperature at the Ta site is larger than at the Sb site. Such differences in site-specific behavior have also been observed in Weyl semimetal TaAs [56]. The origin of the site dependence is unknown, but a theoretical study is warranted.

The power-law coefficient β in the first term is associated with the strength of exchange coupling between lower occupied state where $\beta = 1$ and $\beta = 0$ correspond to purely localized state and delocalized state, respectively. The fit value of $\beta \sim 0.5$, averaged for all sites in TaSb₂, as well as for TaAs [56], may indicate that the assumed in-gap state is rather spatially extended so that the exchange narrowed theory, which predicts $\beta = 1$ may not be applicable. This explanation is on the assumption of in-gap states associated with the Anderson localized or impurity state as a phenomenological description, and the following possibilities for the origin of the upturn can also be mentioned. (i) Contribution from the mobility edge near the gapped band [57], (ii) fluctuations in the Kondo state

(impurity induced Kondo hole) [58], (iii) spin diffusion to the magnetic impurity in topological insulator [59]. Nevertheless, the idea that the nuclear spin diffusion to dilute impurity moments is discussed in YbB₁₂ [59] seems to be one of the plausible interpretations. Likewise, the similar mechanism from bulk to surface metallic state in topological materials is worth investigating from theoretical and experimental viewpoints.

VI. CONCLUDING REMARKS

The presented study is a combination of experimental nuclear quadrupole resonance (NQR) and theoretical calculations using crystal structure obtained from our x-ray single-crystal diffraction. We have reported characteristic static and dynamical properties of observed 13 NQR lines associated with ¹²¹Sb, ¹²³Sb, and ¹⁸¹Ta in TaSb₂. All ^{121/123}Sb and ¹⁸¹Ta NQR lines are successfully assigned to all inequivalent sites and isotopes by combined analysis of the DFT calculation and the WFNMR measurement. The following characteristic features are to be noted.

(i) From the data fitting of the temperature dependence of NQR lines the zero-temperature quadrupole coupling constant ν_Q and asymmetry parameter η are extracted, and those values are in agreement with the DFT calculations within $\pm 16\%$. The temperature dependence of $\nu_Q(T)$ and $\eta(T)$ has been measured up to 250 K, and unusual $\eta(T)$ was observed for the Sb(2) site. The angular dependence of WFNMR frequencies for all sites enabled to determine the direction of the EFG principal axes, V_{xx} and V_{yy} and V_{zz} with respect to the monoclinic crystal axes. The temperature dependencies of the $V_{xx}(T)$ and $V_{yy}(T)$ and $V_{zz}(T)$ have shown a unique characteristic where we found the $V_{yy}(T)$ of Sb(2) site has almost temperature independent. Since the V_{yy} of Sb(2) is pointing exactly to the a axis, the origin of the unexpected $\eta(T)$ may be attributed to the small lattice expansion of the a axis.

(ii) The nuclear relaxation process measured in the NQR at all the sites is proved experimentally by the magnetic excitations, not the quadrupolar. The temperature dependence of relaxation rate, $1/T_1T(T)$, has quite characteristic behavior similar to the many semimetal materials. That is the high-temperature activation type process crosses over to the low-temperature excess relaxation process, making an upturn in $1/T_1T(T)$ around 30–70 K. However, neither high- nor low-temperature behaviors could be explained by the simple Fermi liquid using the DFT density of states at Fermi level, even the temperature dependence of the chemical potential is included. Followed by the traditional procedure, the activation-type behavior of $1/T_1T(T)$ was analyzed by assuming simple in gap state could reproduce high temperature $1/T_1T(T)$. This energy scale of the activation is similar to other topological materials. We did not observe any power-law behavior in $1/T_1T(T)$ characteristic to Weyl or Dirac fermion excitations.

Our DFT-supported NQR/NMR study with the local probes Ta and Sb provide with a valuable contribution to understanding of the temperature-dependent local charge distribution, band structure, and magnetic excitations in the topological semimetal TaSb₂.

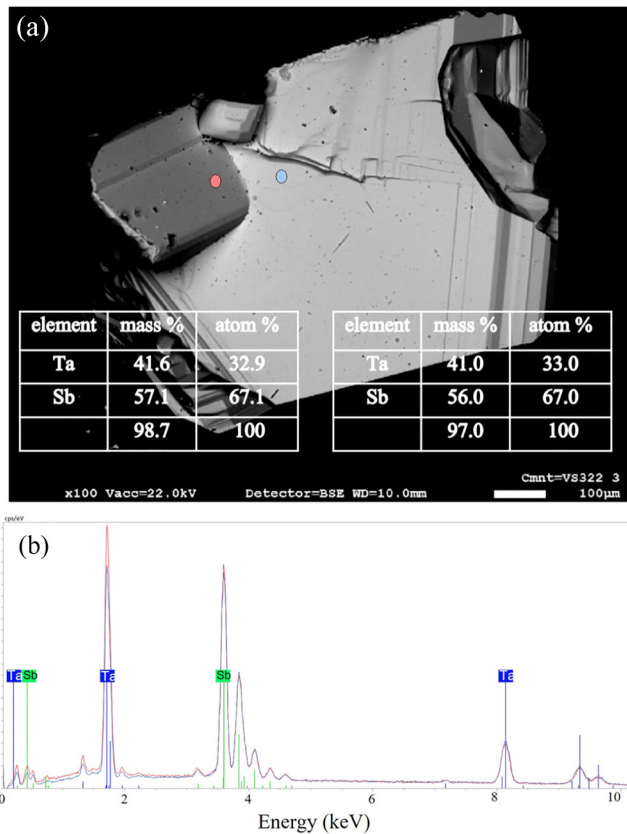


FIG. 9. (a) Back scattered electron (BSE) image of as grown crystals. The chemical composition (see Tables) are determined by semiquantitative EDX method. (b) Energy-dispersive x-ray spectra [color refers to electron beam position in a)].

ACKNOWLEDGMENTS

O.J. and H.R. thank U. Nitzsche for technical assistance. We thank V. Hasse for technical support in the characterization and synthesis of the samples.

APPENDIX A: SAMPLE CHARACTERIZATION (EDX AND XRD)

The chemical composition of the as-grown TaSb₂ crystals have been determined by energy dispersive x-ray spectroscopy (EDXS) in a scanning electron microscope (Jeol JSM 7800F) as shown in Fig. 9. Measurements with an acceleration voltage of 22 kV result in an analytical totals of more than 97 mass % by using the ZAF matrix correction model for the calculation of the mass concentration from the intensities of the x-ray lines Sb L α (3.6 keV) and Ta L α (8.1 keV). The respective element ratio does not deviate significantly from formal concentration of Ta: 33.3 at.%, Sb: 66.6 at.%. X-ray intensities are measured with the silicon drift detector (Bruker Esprit ver.2.3 EDX system) attached to the SEM. The crystal structure investigation of TaSb₂ was carried out by using x-ray single-crystal diffraction. Suitable specimen for the investigation was mechanically extracted from larger crystal grown by chemical transport. Intensity data collection was performed by using Rigaku AFC7 diffractometer equipped by Saturn 724+ CCD detector (MoK α radiation). Structural

TABLE III. Crystallographic data for TaSb₂.

Composition	TaSb ₂
Space group	<i>C2/m</i>
Pearson symbol	<i>mS12</i>
Formula units per unit cell, Z	4
Lattice parameters	
$a/\text{\AA}$	10.233(2)
$b/\text{\AA}$	3.6487(5)
$c/\text{\AA}$	8.3036(19)
$\beta/^\circ$	120.40(1)
$V/\text{\AA}^3$	267.41(9)
Cal. density/ gcm^{-3}	10.54
Crystal form	irregular shaped
Crystal size/ μm	$0.030 \times 0.035 \times 0.060$
Diffraction system	RIGAKU AFC7
Detector	Saturn 742 + CCD
Radiation, $\lambda/\text{\AA}$	MoK α , 0.71073
Scan; step/degree; N(images)	ϕ , 0.8, 900
Maximal $2\theta/\text{degree}$	78.0
Range in h, k, l	$-18 \leq h \leq 17$ $-6 \leq k \leq 4$ $-14 \leq l \leq 10$
Absorption correction	multiscan
$T(\text{max})/T(\text{min})$	0.453
Absorption coeff./ mm^{-1}	60.5
$N(hkl)$ measured	2509
$N(hkl)$ unique	847
R_{int}	0.041
$N(hkl)$ observed	812
Observation criteria	$F(hkl) \geq 4\sigma(F)$
Refined parameters	20
$R1$	0.028
$wR2$	0.067
Residual peaks/ $e \text{\AA}^{-3}$	-5.00/4.68

model with one Ta and two Sb crystallographic positions (all in 4i Wyckoff sites) was refined in the space group *C2/m* [$a = 10.233(2) \text{\AA}$, $b = 3.6487(5) \text{\AA}$, $c = 8.3036(19) \text{\AA}$, $\beta = 120.40(1)^\circ$, $R1 = 0.028$, $wR2 = 0.067$] more detail is seen in Table III. In separate cycle of the refinement procedure, the occupancy factors of all atomic positions were allowed to vary freely. This showed no deviation from the ideal values, confirming the 1:2 stoichiometry of the examined sample. The final runs were implemented with the full (fixed) occupancies for all atomic positions (see Tables IV, V). The least-squares fit of the experimental x-ray powder pattern to that calculated from the obtained structural model showed good agreement (Fig. 10), indicating high purity of the synthesized material.

TABLE IV. Atomic coordinates and equivalent displacement parameters (in \AA^2) in the crystal structure of TaSb₂.

Atom	site	x/a	y/b	z/c	U_{eq}
Ta	4i	0.15151(3)	0	0.18914(3)	0.00492(11)
Sb(1)	4i	0.40541(5)	0	0.11318(6)	0.00578(11)
Sb(2)	4i	0.14706(5)	0	0.53391(6)	0.00602(11)

TABLE V. Anisotropic displacement parameters (in \AA^2) in the crystal structure of TaSb₂. $U_{12} = U_{23} = 0$.

Atom	U_{11}	U_{22}	U_{33}	U_{13}
Ta	0.00531(14)	0.00481(15)	0.00437(15)	0.00225(10)
Sb(1)	0.00657(19)	0.00509(19)	0.0062(2)	0.00361(15)
Sb(2)	0.00621(19)	0.00608(19)	0.00562(19)	0.00289(15)

APPENDIX B: RECOVERY OF NUCLEAR MAGNETIZATION

For the magnetic relaxation, the time dependence of the recovery of nuclear magnetization measured by NQR intensity should obey Eqs. (B1) and (B2) for $I = 5/2$ (^{121}Sb) and $I = 7/2$ (^{123}Sb and ^{181}Ta), respectively [60].

$$M_{I=5/2} = M_0 \left[1 - c_0 \left(Q_1 \exp \frac{-K_1 t}{T_1} + Q_2 \exp \frac{-K_2 t}{T_1} \right) \right], \quad (\text{B1})$$

$$M_{I=7/2} = M_0 \left[1 - c_0 \left(Q_1 \exp \frac{-K_1 t}{T_1} + Q_2 \exp \frac{-K_2 t}{T_1} + Q_3 \exp \frac{-K_3 t}{T_1} \right) \right], \quad (\text{B2})$$

where c_0 is the degree of inversion, and Q_n ($n = 1, 2, 3$) and K_n ($n = 1, 2, 3$) are the parameters depending on the nuclear spin I and η . All parameters are calculated in Ref. [60] for a given I and η . The typical examples are shown in Fig. 11, where the experimental recovery curves for the f_2 lines in $^{121}\text{Sb}(1)$, $^{121}\text{Sb}(2)$, and ^{181}Ta NQR lines are shown with the best fit curve to Eqs. (B1) and (B2) using K_n and Q_n shown in Table VI. The obtained perfect fit provides us with the relaxation process is governed by the magnetic fluctuations.

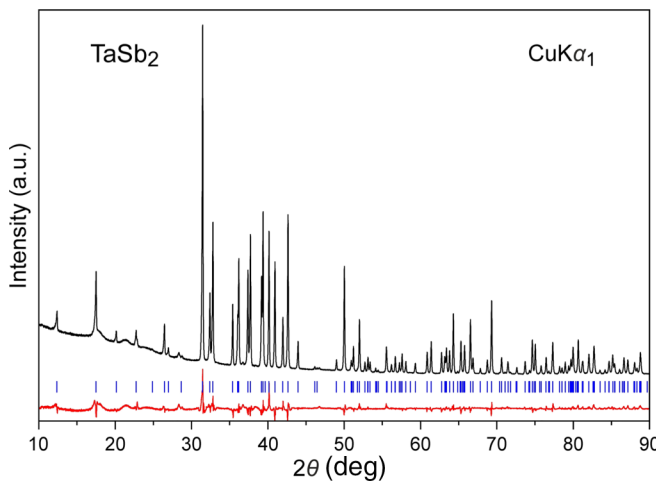


FIG. 10. X-ray powder diffraction recorded in Guinier geometry (black line). The difference between measured and calculated intensities is represented as a red curve. Blue vertical bars indicate reflection positions of the refined model.

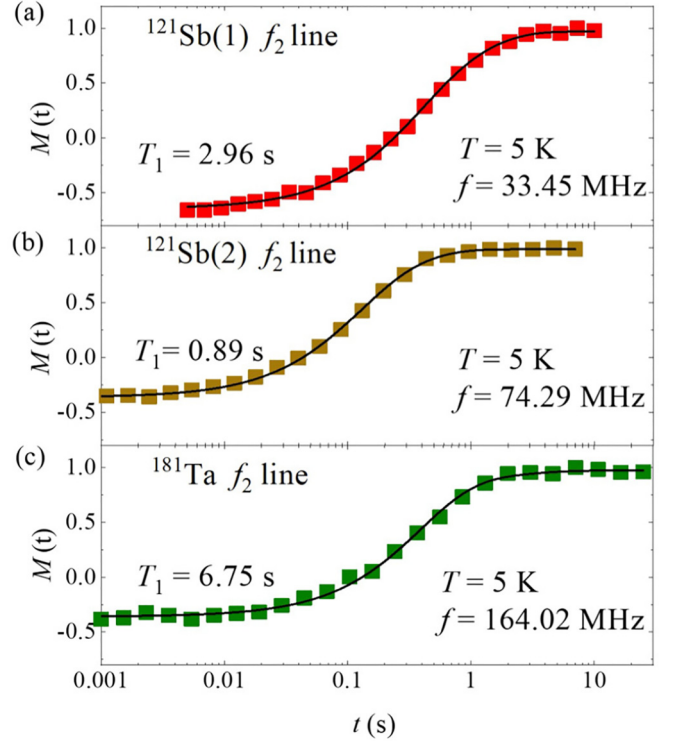


FIG. 11. Recovery of nuclear magnetization $M(t)$ measured by the spin-echo amplitude after an inversion pulse for ^{121}Sb [(a) and (b)] and ^{181}Ta [(c)] NQR lines at 5 K. The black solid lines are data fits to Eqs. (B1) and (B2) for ^{121}Sb and ^{181}Ta , respectively.

APPENDIX C: ANGULAR DEPENDENCE OF Δf

When we apply H to the sample, we treat the Zeeman term $H_z = -\gamma_N H (I_x \sin \theta \cos \phi + I_z \cos \theta)$ as the perturbation of H_Q . Then the Hamiltonian is modified as follows,

$$\begin{aligned} \langle m | H_Q + H_z | m \rangle = & \left[-m \hbar \gamma_N H \cos \theta \right. \\ & + \frac{e^2 Q}{6I(2I-1)} \left[\{3m^2 - I(I+1)\} \right. \\ & \left. \left. \times \left\{ V_{zz} - \frac{1}{2}(V_{xx} - V_{yy}) \right\} \right] \right] \langle m | m \rangle, \quad (\text{C1}) \end{aligned}$$

TABLE VI. The calculated prefactors Q_n and exponent K_n in Eqs. (B1) and (B2) for $\eta = 0.42$, $\eta = 0.74$, and $\eta = 0.32$ for $^{121}\text{Sb}(1)$, $^{121}\text{Sb}(2)$, and ^{181}Ta [60].

$^{121}\text{Sb}(1)$	$K_1 = 3.0215, K_2 = 8.9861$		
f_1 line	$Q_1 = 0.1432$	$Q_2 = 0.8568$	
f_2 line	$Q_1 = 0.3783$	$Q_2 = 0.6217$	
$^{121}\text{Sb}(2)$	$K_1 = 3.0444, K_2 = 8.1479$		
f_1 line	$Q_1 = 0.1972$	$Q_2 = 0.8028$	
f_2 line	$Q_1 = 0.3085$	$Q_2 = 0.6915$	
^{181}Ta	$K_1 = 3.0645, K_2 = 9.2297, K_3 = 18.2449$		
f_1 line	$Q_1 = 0.0441$	$Q_2 = 0.4015$	$Q_3 = 0.5544$
f_2 line	$Q_1 = 0.0862$	$Q_2 = 0.0584$	$Q_3 = 0.8554$
f_3 line	$Q_1 = 0.2032$	$Q_2 = 0.5526$	$Q_3 = 0.2442$

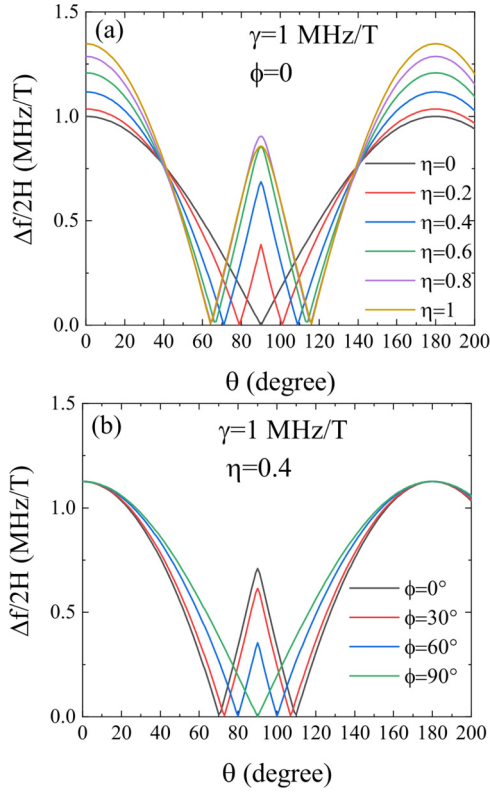


FIG. 12. Angular dependence of $\Delta f/2H$ calculated using the exact diagonalization of Eqs. (C1), (C2) and (C3) (a) for $\eta = 0 \sim 1$ (b) $\phi = 0 \sim 90$ degree.

$$\begin{aligned} & \langle m \pm 1 | H_Q + H_z | m \rangle \\ &= \mp \frac{1}{2} \gamma_N H \sqrt{I(I+1) - m(m \pm 1)} \sin \theta \cos \phi \langle m | m \rangle, \end{aligned} \quad (\text{C2})$$

$$\begin{aligned} & \langle m \pm 2 | H_z + H_Q | m \rangle \\ &= \left[\frac{e^2 Q}{6I(2I-1)} \left[\frac{3}{4} (V_{xx} - V_{yy}) \sqrt{I(I+1) - m(m \pm 1)} \right. \right. \\ & \quad \left. \left. \times \sqrt{I(I+1) - (m \pm 1)(m \pm 2)} \right] \right] \langle m | m \rangle. \end{aligned} \quad (\text{C3})$$

We obtain nuclear energy levels, E_m , by the Zeeman effect resulting from the exact diagonalization of matrix, which consists of Eqs. (C1), (C2), and (C3). When $\eta = 0$ and $\theta = 0$ ($H \parallel V_{zz}$), WFNMR occurs for the transition between two levels m and $m \pm 1$ ($|m| > 3/2$), and the resonance frequency can be expressed as, $f_{\pm m}^{\text{WFNMR}} = \nu_{\text{NQR}} \pm \gamma_N H$.

Following Eqs. (C1), (C2), and (C3), we know that a measurement of the angular dependence of $\Delta f/2H$ makes it possible to determine the principal axis direction of V_{zz} (θ and ϕ) and η . We have calculated the angular dependence of $\Delta f/2H$ using the exact diagonalization of Eqs. (C1), (C2), and (C3). Here, we assume that V_{zz} is along $\theta = 0^\circ$, $\phi = 0^\circ$, and $\gamma = 1$ MHz/T. The maximum of $\Delta f/2H$ increases with η , as shown in Fig. 12(a). And the $\Delta f/2H$ at 90° also changes

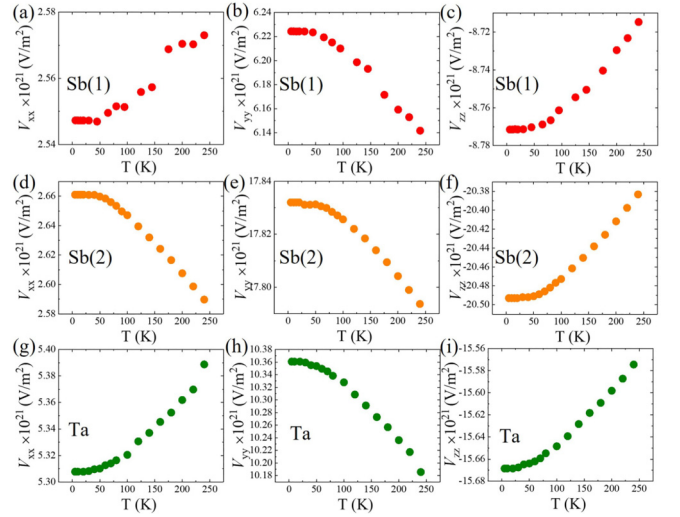


FIG. 13. Temperature dependence of EFG tensor V_{xx} , V_{yy} and V_{zz} at (a), (b), (c) Sb(1), (d), (e), (f) Sb(2), and (g), (h), (i) Ta site.

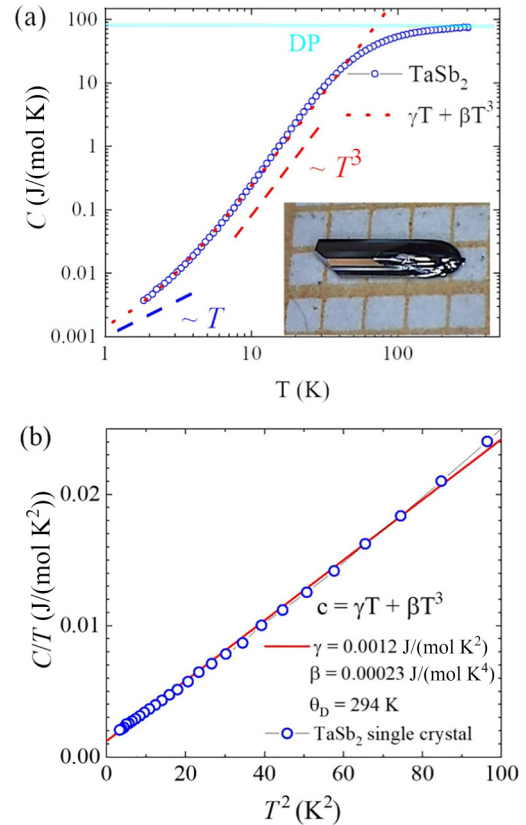


FIG. 14. (a) Specific heat as a function of temperature. DP denotes the Dulong-Petit value. The curved dotted line indicates a description of the data below 10 K with electron and phonon contribution. (b) Plot of the specific heat C/T versus T^2 . The straight line indicates a description with electron and phonon contribution. The intercept at $T = 0$ indicates an electronic contribution to the specific heat.

with η . On the other hand, Fig. 12(b) shows that ϕ has no effect on the maximum value of $\Delta f/2H$, but the 90° component decreases with ϕ . Therefore, the direction of V_{zz} and η can be obtained by analyzing the experimental results of the angular dependence of $\Delta f/2H$ using a least-squares analysis with η and ϕ as parameters.

APPENDIX D: TEMPERATURE DEPENDENCE OF EFG TENSOR

To examine the EFG tensor in detail, V_{xx} , V_{yy} , and V_{zz} were obtained by decomposing the temperature dependence of $\nu_Q(T)$ and $\eta(T)$. The $V_{zz}(T)$ was determined based on Eq. (2) in the main text, and the sign was determined by the DFT calculation (see in Table II). Since the EFG tensor is defined as $|V_{zz}| > |V_{yy}| > |V_{xx}|$ and $V_{zz} + V_{yy} + V_{xx} = 0$, V_{xx} and V_{yy} can be written as $V_{xx} = V_{zz}(\eta-1)/2$ and $V_{yy} = -V_{zz}(\eta + 1)/2$.

Thus we determined $V_{xx}(T)$, $V_{yy}(T)$, and $V_{zz}(T)$ for each site are shown in Figs. 13(a)–13(i).

APPENDIX E: SPECIFIC HEAT

The specific heat of a TaSb₂ single crystal was measured in the temperature range between 2 K and 300 K using Quantum Design PPMS system (Fig. 14). At high temperatures, the Dulong-Petit law was proven. At low temperatures, the data can be described with a linear (electron) and a cubic (phonon) dependence. It is clear that (i) there is no increase in C/T , which means the increase in $1/T_1T$ at low temperatures may not be electron origin and (ii) the determined value for the linear part is 1.2 mJ/molK², which is within the range of what is estimated from the band-structure calculations [Fig. 2(b) in the main text].

-
- [1] A. H. CastroNeto, F. Guinea, N. M. R. Peres, K. S. Novoselov, and A. K. Geim, *Rev. Mod. Phys.* **81**, 109 (2009).
- [2] C. L. Kane and E. J. Mele, *Phys. Rev. Lett.* **95**, 146802 (2005).
- [3] B. A. Bernevig, T. L. Hughes, and S.-C. Zhang, *Science* **314**, 1757 (2006).
- [4] M. Z. Hasan and C. L. Kane, *Rev. Mod. Phys.* **82**, 3045 (2010).
- [5] T. O. Wehling, A. M. Black-Schaffer, and A. V. Balatsky, *Adv. Phys.* **63**, 1 (2014).
- [6] N. P. Armitage, E. J. Mele, and A. Vishwanath, *Rev. Mod. Phys.* **90**, 015001 (2018).
- [7] B. Yan and C. Felser, *Annu. Rev. Condens. Matter Phys.* **8**, 337 (2017).
- [8] S.-Y. Xu, I. Belopolski, N. Alidoust, M. Neupane, G. Bian, C. Zhang, R. Sankar, G. Chang, Z. Yuan, C.-C. Lee, S.-M. Huang, H. Zheng, J. Ma, D. Sanchez, B. Wang, A. Bansil, F. Chou, P. Shibaev, H. Lin, S. Jia, and M. Z. Hasan, *Science* **349**, 613 (2015).
- [9] B. Q. Lv, H. M. Weng, B. B. Fu, X. P. Wang, H. Miao, J. Ma, P. Richard, X. C. Huang, L. X. Zhao, G. F. Chen, Z. Fang, X. Dai, T. Qian, and H. Ding, *Phys. Rev. X* **5**, 031013 (2015).
- [10] C. Shekhar, A. K. Nayak, Y. Sun, M. Schmidt, M. Nicklas, I. Leermakers, U. Zeitler, Y. Skourski, J. Wosnitza, Z. Liu, Y. Chen, W. Schnelle, H. Borrmann, Y. Grin, C. Felser, and B. Yan, *Nature Phys.* **11**, 645 (2015).
- [11] T. Liang, Q. Gibson, M. N. Ali, M. Liu, R. Cava, and N. Ong, *Nature Mater.* **14**, 280 (2015).
- [12] A. Narayanan, M. D. Watson, S. F. Blake, N. Bruyant, L. Drigo, Y. L. Chen, D. Prabhakaran, B. Yan, C. Felser, T. Kong, P. C. Canfield, and A. I. Coldea, *Phys. Rev. Lett.* **114**, 117201 (2015).
- [13] X. Huang, L. Zhao, Y. Long, P. Wang, D. Chen, Z. Yang, H. Liang, M. Xue, H. Weng, Z. Fang, X. Dai, and G. Chen, *Phys. Rev. X* **5**, 031023 (2015).
- [14] J. Hu, J. Liu, D. Graf, S. Radmanesh, D. Adams, A. Chuang, Y. Wang, I. Chiorescu, J. Wei, L. Spinu, and Z. Q. Mao, *Sci. Rep.* **6**, 18674 (2016).
- [15] J. Klotz, S.-C. Wu, C. Shekhar, Y. Sun, M. Schmidt, M. Nicklas, M. Baenitz, M. Uhlarz, J. Wosnitza, C. Felser, and B. Yan, *Phys. Rev. B* **93**, 121105(R) (2016).
- [16] F. Arnold, C. Shekhar, S.-C. Wu, Y. Sun, R. D. Dos Reis, N. Kumar, M. Naumann, M. O. Ajeesh, M. Schmidt, A. G. Grushin, J. H. Bardarson, M. Baenitz, D. Sokolov, H. Borrmann, M. Nicklas, C. Felser, E. Hassinger, and B. Yan, *Nat. Commun.* **7**, 11615 (2016).
- [17] T. Besara, D. A. Rhodes, K.-W. Chen, S. Das, Q. R. Zhang, J. Sun, B. Zeng, Y. Xin, L. Balicas, R. E. Baumbach, E. Manousakis, D. J. Singh, and T. Siegrist, *Phys. Rev. B* **93**, 245152 (2016).
- [18] S.-I. Kimura, H. Yokoyama, H. Watanabe, J. Sichelschmidt, V. Süß, M. Schmidt, and C. Felser, *Phys. Rev. B* **96**, 075119 (2017).
- [19] B. Xu, Y. M. Dai, L. X. Zhao, K. Wang, R. Yang, W. Zhang, J. Y. Liu, H. Xiao, G. F. Chen, A. J. Taylor, D. A. Yarotski, R. P. Prasankumar, and X. G. Qiu, *Phys. Rev. B* **93**, 121110(R) (2016).
- [20] S.-I. Kimura, Y. Nakajima, Z. Mita, R. Jha, R. Higashinaka, T. D. Matsuda, and Y. Aoki, *Phys. Rev. B* **99**, 195203 (2019).
- [21] H. Weng, C. Fang, Z. Fang, B. A. Bernevig, and X. Dai, *Phys. Rev. X* **5**, 011029 (2015).
- [22] S.-M. Huang, S.-Y. Xu, I. Belopolski, C.-C. Lee, G. Chang, B. Wang, N. Alidoust, G. Bian, M. Neupane, C. Zhang, C. Zhang, S. Jia, A. Bansil, H. Lin, and M. Z. Hasan, *Nature Commun.* **6**, 7373 (2015).
- [23] Y. Zhou, B. Li, Z. Lou, H. Chen, Q. Chen, B. Xu, C. Wu, J. Du, J. Yang, H. Wang, and M. Fang, *Sci. China Phys. Mech. Astron.* **64**, 247411 (2021).
- [24] M. Baenitz, M. Schmidt, V. Suess, C. Felser, and K. Lüders, *J. Phys.: Conf. Ser.* **1293**, 012002 (2019).
- [25] Y. Qi, P. G. Naumov, M. N. Ali, C. R. Rajamathi, W. Schnelle, O. Barkalov, M. Hanfland, S. C. Wu, C. Shekhar, Y. Sun, Vicky Süß, M. Schmidt, U. Schwarz, E. Pippel, P. Werner, R. Hillebrand, T. Förster, E. Kampert, S. Parkin, R. J. Cava, C. Felser, B. Yan, and S. A. Medvedev, *Nat. Commun.* **7**, 11038 (2016).
- [26] A. Ikeda, M. Kawaguchi, S. Koibuchi, T. Hashimoto, T. Kawakami, S. Yonezawa, M. Sato, and Y. Maeno, *Phys. Rev. Mater.* **4**, 041801(R) (2020).

- [27] H. Takahashi, S. Kitagawa, K. Ishida, M. Kawaguchi, A. Ikeda, S. Yonezawa, and Y. Maeno, *J. Phys. Soc. Jpn.* **90**, 073702 (2021).
- [28] B. Shen, X. Deng, G. Kotliar, and N. Ni, *Phys. Rev. B* **93**, 195119 (2016).
- [29] Y. Li, L. Li, J. Wang, T. Wang, X. Xu, C. Xi, C. Cao, and J. Dai, *Phys. Rev. B* **94**, 121115(R) (2016).
- [30] A. C. Niemann, J. Gooth, S.-C. Wu, S. Bäßler, P. Sergelius, R. Hühne, B. Rellinghaus, C. Shekhar, V. Süß, M. Schmidt, C. Felser, B. Yan, and K. Nielsch, *Sci. Rep.* **7**, 43394 (2017).
- [31] C. Xu, J. Chen, G.-X. Zhi, Y. Li, J. Dai, and C. Cao, *Phys. Rev. B* **93**, 195106 (2016).
- [32] D. Gresch, Q. Wu, G. W. Winkler, and A. A. Soluyanov, *New J. Phys.* **19**, 035001 (2017).
- [33] H. Yasuoka, T. Kubo, Y. Kishimoto, D. Kasinathan, M. Schmidt, B. Yan, Y. Zhang, H. Tou, C. Felser, A. P. Mackenzie, and M. Baenitz, *Phys. Rev. Lett.* **118**, 236403 (2017).
- [34] Y. Tian, N. Ghassemi, and J. H. Ross Jr, *Phys. Rev. B* **102**, 165149 (2020).
- [35] Y. Tian, N. Ghassemi, and J. H. Ross Jr, *Phys. Rev. B* **100**, 165149 (2019).
- [36] T. Yokoo, Y. Watanabe, M. Kumazaki, M. Itoh, and Y. Shimizu, *J. Phys. Soc. Jpn.* **91**, 054701 (2022).
- [37] A. Antonenko, E. Charnaya, A. Pirozerskii, D. Y. Nefedov, M.-K. Lee, L. Chang, J. Haase, S. Naumov, A. Domozhireva, and V. Marchenkov, *Res. Phys.* **21**, 103793 (2021).
- [38] C. G. Wang, Y. Honjo, L. Zhao, G. F. Chen, K. Matano, R. Zhou, and G.-Q. Zheng, *Phys. Rev. B* **101**, 241110(R) (2020).
- [39] H. Maebashi, T. Hirose, M. Ogata, and H. Fukuyama, *J. Phys. Chem. Solids* **128**, 138 (2019).
- [40] Z. Okvátovity, H. Yasuoka, M. Baenitz, F. Simon, and B. Dóra, *Phys. Rev. B* **99**, 115107 (2019).
- [41] F. Hulliger, *Nature (London)* **204**, 775 (1964).
- [42] G. Saini, L. Calvert, and J. Taylor, *Can. J. Chem.* **42**, 630 (1964).
- [43] S. Furuseth, K. Selte, A. Kjekshus, S. Gronowitz, R. Hoffman, and A. Westerdahl, *Acta Chem. Scand* **19**, 42 (1965).
- [44] K. Koepf and H. Eschrig, *Phys. Rev. B* **59**, 1743 (1999).
- [45] J. P. Perdew and Y. Wang, *Phys. Rev. B* **45**, 13244 (1992).
- [46] The Materials Project, Materials Data on TaSb₂ by Materials Project, United States, 2020, doi:10.17188/1188289.
- [47] T. P. DAS and E. L. Hahn, *Nuclear Quadrupole Resonance Spectroscopy* (Springer, Berlin, 1958).
- [48] J. Christiansen, P. Heubes, R. Keitel, W. Klinger, W. Loeffler, W. Sandner, and W. Witthuhn, *Z. Phys. B Cond. Matt.* **24**, 177 (1976).
- [49] Z. Okvátovity, F. Simon, and B. Dóra, *Phys. Rev. B* **94**, 245141 (2016).
- [50] A. Narath and H. Weaver, *Phys. Rev.* **175**, 373 (1968).
- [51] T. Moriya, *J. Phys. Soc. Jpn.* **18**, 516 (1963).
- [52] C. P. Slichter, *Principles of Magnetic Resonance*, 3rd ed. (Springer, New York, 1990), p. 151.
- [53] M. Takigawa, H. Yasuoka, Y. Kitaoka, T. Tanaka, H. Nozaki, and Y. Ishizawa, *J. Phys. Soc. Jpn.* **50**, 2525 (1981).
- [54] A. Dioguardi, H. Yasuoka, S. Thomas, H. Sakai, S. Cary, S. Kozimor, T. Albrecht-Schmitt, H. Choi, J.-X. Zhu, J. Thompson, E. Bauer, and F. Ronnig, *Phys. Rev. B* **99**, 035104 (2019).
- [55] A. A. Gippius, V. Y. Verchenko, A. V. Tkachev, N. E. Gervits, C. S. Lue, A. A. Tsirlin, N. Büttgen, W. Krätschmer, M. Baenitz, M. Shatruk, and A. V. Sevelkov, *Phys. Rev. B* **89**, 104426 (2014).
- [56] T. Kubo, H. Yasuoka, B. Dóra, D. Kasinathan, Y. Prots, H. Rosner, T. Fujii, M. Schmidt, and M. Baenitz, *J. Phys. Soc. Jpn.* **92**, 094706 (2023).
- [57] P. Schlottmann, *Phys. Rev. B* **90**, 165127 (2014).
- [58] T. Caldwell, A. P. Reyes, W. G. Moulton, P. L. Kuhns, M. J. R. Hoch, P. Schlottmann, and Z. Fisk, *Phys. Rev. B* **75**, 075106 (2007).
- [59] N. Shishiuchi, Y. Kato, O. M. Vyaselev, M. Takigawa, S. Hiura, F. Iga, and T. Takabatake, *J. Phys. Chem. Solids* **63**, 1231 (2002).
- [60] J. Chepin Jr and J. H. Ross Jr, *J. Phys.: Condens. Matter* **3**, 8103 (1991).